

ACCRETION DISKS AROUND YOUNG OBJECTS. III. GRAIN GROWTH

Paola D'Alessio^{1,2}, Nuria Calvet³, and Lee Hartmann³

ABSTRACT

We present detailed models of irradiated T Tauri disks including dust grain growth with power-law size distributions. The models assume complete mixing between dust and gas and solve for the vertical disk structure self-consistently including the heating effects of stellar irradiation as well as local viscous heating. For a given total dust mass, grain growth is found to decrease the vertical height of the surface where the optical depth to the stellar radiation becomes unit and thus the local irradiation heating, while increasing the disk emission at mm and sub-mm wavelengths. The resulting disk models are less geometrically thick than our previous models assuming interstellar medium dust, and agree better with observed spectral energy distributions and images of edge-on disks, like HK Tau/c and HH 30. The implications of models with grain growth for determining disk masses from long-wavelength emission are considered.

Subject headings: Physical data and processes: accretion, accretion disks — stars: circumstellar matter, formation, pre-main sequence

1. Introduction

It has been clear for more than a decade that the absorbing surfaces or photospheres of T Tauri disks had to be “flared”, i.e. curved upward away from the disk midplane, to explain the typical observed spectral energy distribution at infrared wavelengths (Kenyon & Hartmann 1987). Because of flaring, the irradiation of the disk by the central star tends to dominate the disk heating at large radii (Calvet et al. 1992). Since the amount of flaring depends upon the temperature structure, which in turn depends upon the flaring-dependent irradiation, the self-consistent structure in general must be solved iteratively (Kenyon & Hartmann 1987; D’Alessio 1996; D’Alessio et al. 1998, 1999a). The dust grains control the absorption and emission of radiation and therefore the knowledge of their properties help determine the disk structure.

¹Department of Astrophysics, American Museum of Natural History, Central Park West at 79th Street, New York, NY 10024-5192; Electronic mail: paola@amnh.org

²Instituto de Astronomía, UNAM, Ap. Postal 70-264, Cd. Universitaria, 04510 México D.F., México

³Harvard-Smithsonian Center for Astrophysics, 60 Garden St., Cambridge, MA 02138, USA; Electronic mail: hartmann@cfa.harvard.edu, ncalvet@cfa.harvard.edu

In a previous paper (D’Alessio et al. 1999b = Paper II), we constructed models for T Tauri disks in which the vertical disk structure was self-consistently solved assuming well-mixed dust with properties characteristic of interstellar grains. We found that the resulting models were too geometrically thick, which is also the case of the two-layer flared disk models of Chiang & Goldreich (1997, 1999). Our models also exhibited too little mm- and sub-mm wavelength emission, in comparison with observations. These deficiencies can in principle be relieved or eliminated by models including grain growth and settling to the disk midplane, processes which are thought to be essential precursors to planet formation (e.g., Beckwith, Henning & Nakagawa 2000). Even without settling, grain growth alone can help improve the comparison with observations, since for a given dust mass growth can increase the long-wavelength opacity at the same time it decreases the optical-near infrared opacity; the latter effect reduces the apparent disk thickness at short wavelengths, and can even reduce the true disk vertical scale height by reducing irradiation heating.

It is generally thought that some grain growth must have occurred in T Tauri disks to explain the spectral indices of the long-wavelength disk emission in some systems (Beckwith & Sargent 1991 = BS91; Mannings & Emerson 1994; Pollack, et al. 1994 = P94). Unfortunately, the details of this process are poorly understood. We are therefore motivated to adopt a parameterized approach with few parameters to make an initial exploration of the effects of dust growth on T Tauri disk structure.

In this paper we present sequences of detailed, physically self-consistent disk models with power-law distributions of dust particle sizes. We find that modest grain growth substantially improves comparison with spectral energy distributions (SEDs) and optical-near infrared imaging. Using both observed mm-wave fluxes and spectral slopes as constraints, we suggest limits on the maximum grain size in some systems. Our results emphasize the importance of optical depth effects in constraining disk properties, and suggest observational tests which might ultimately lead to more accurate disk masses. The presence of silicate emission may require differential distributions of small and large dust, i.e., settling of large grains to midplane with small grains (size $< 10 \mu\text{m}$) at larger heights. This issue will be addressed in a forthcoming paper of this series.

2. Dust opacities

Dust is the most important opacity source in T Tauri disk models, and controls the temperature distribution within the disk as well as the emissivity at long wavelengths. We adopt the model of dust for disks proposed by P94, with a few variations. We assume that the optical properties of olivine and orthopyroxene are represented by the “astronomical silicates” (Draine & Lee 1984), i.e., crystalline olivine with dielectric functions given by Laor & Draine (1993) and Weingartner & Draine (2000). However, following P94, the imaginary refractive index is taken to be constant for $\lambda > 800 \mu\text{m}$, for consistency with laboratory measurements (Campbell & Ulrichs 1969; Henning & Stognienko 1996). The optical constants of water ice are taken from Warren

1984. Refractive indices for troilite are taken from Begemann et al. (1994) (see Henning et al. 1999) for $10 < \lambda < 500 \mu\text{m}$ and from P94 for other wavelengths. Finally, the refractive indices of organics are taken from P94. The mass fractional abundances of these dust species respect to gas are $\zeta_{sil} = 0.0034$, $\zeta_{tro} = 0.000768$, $\zeta_{ice} = 0.0056$, and $\zeta_{org} = 0.0041$, and their bulk densities are $\rho_{sil} = 3.3$, $\rho_{tro} = 4.83$, $\rho_{ice} = 0.92$ and $\rho_{org} = 1.5 \text{ g cm}^{-3}$, respectively, consistent with P94. The sublimation temperature of each of these species is taken from P94.

The efficiency factor Q_{abs} is calculated using a Mie scattering code (Wiscombe 1979, updated in 1996), assuming that the grains are spheres. Coagulation tends to produce grains which are not compact spheres, but rather aggregates with a porous structure and a bulk density that decreases with size (Meakin & Donn 1988). The shapes of these grains are affected by different kind of processes which may take place in the disk, such as turbulence, settling, radial drift, etc.; in turn, the optical properties of these aggregates depend on their complex shapes (e.g., Henning & Stognienko 1996; Beckwith, Henning & Nakagawa 2000). However, in the relatively dense environment of a circumstellar disk, there are frequent collisions between particles and a strong interaction with the surrounding gas, tending to produce erosion and compaction of grains (Miyake & Nakagawa 1993 = MN93). In any event, for simplicity and lacking any detailed description of the shapes and optical properties of grains in turbulent disks, we assume that the disk grains interact with light as compact segregated spheres.

The size distribution of dust grains is taken to be a power law $n(a) = n_0 a^{-p}$, where a is the grain radius, n_0 is a normalization constant and the exponent p is a free parameter. Approximate justification for this is taken from the calculations of Weidenschilling (1997), who finds a wide range of dust sizes at any given time due to a combination of grain growth and shattering. We assume a minimum grain radius $a_{min} = 0.005 \mu\text{m}$ and different maximum size a_{max} and exponent p . Table 1 summarizes representative values of the opacity and albedo at different wavelengths for various a_{max} and p . In this paper we use the following notation: κ_ν is the mass absorption coefficient (i.e., corresponding to “true absorptions”), χ_ν is the total extinction coefficient (i.e., absorptions plus scattering) and w_ν is the albedo (given by $w_\nu = 1 - \kappa_\nu/\chi_\nu$). For comparison, we frequently refer to “ISM-dust”, which corresponds to abundances and optical properties from Draine & Lee (1984), i.e., “astronomical silicates” and graphite, with $a_{max} = 0.25 \mu\text{m}$ and $p = 3.5$.

Figure 1 shows the opacity as a function of wavelength for dust grain size distributions with $p = 2.5$ and 3.5 , and maximum size $a_{max} = 10 \mu\text{m}$, 1 mm and 10 cm , for temperatures $T = 100$ and 300 K (i.e., with and without water ice, respectively). For a given value of p , when the maximum grain size increases, the opacity at small wavelengths ($\lambda \lesssim a_{max}$) decreases and the opacity at larger wavelengths increases. Since the dust to gas mass ratio is assumed to be constant and the mass in grains is dominated by the bigger grains if $p < 4$ (MN93), a larger a_{max} implies a smaller mass in small grains which are the most efficient absorbing radiation in the visible and near-IR. At the same time, as a_{max} increases, the transition between the geometrical and optical regimes occurs at longer wavelengths ($\sim 2\pi a_{max}$), so that the opacity at $\lambda \sim a_{max}$ increases. In Table 1 we show the Planck mean opacities characteristic of the stellar radiation κ_P^* and χ_P^* , both calculated

using the Planck function evaluated at a typical stellar temperature $T_* = 4000$ K (see paper II). These values are similar to the monochromatic coefficient evaluated at $\lambda \sim 1 \mu m$, and are used to calculate the disk heating by stellar radiation (see paper II for details). The table illustrates how these mean opacities also decrease with a_{max} . The consequences of this behavior for the disk structure and emission properties will be discussed in §4.

Figure 2 shows the contribution of the different grains to the absorption coefficient for $T = 100$ K, $a_{max} = 1 \mu m$ and 1 mm and $p = 2.5$ and 3.5. In general, the relative contribution of each type of grain depends on the wavelength and size distribution. For $a_{max} = 1$ mm, silicates are the most important contributor at $\lambda \sim 1$ mm, and troilite becomes of comparable importance in the cm range. In the mid- and far-IR range, water ice dominates, and the second important contributor are organics. For $a_{max} = 1 \mu m$, silicates dominates the opacity in the mm and cm range, and troilite is not very important. In the mid- and far-IR water ice is dominant, with important contributions of silicates and organics. In particular, the organics tend to increase the opacity at $\lambda \lesssim 6 \mu m$, decreasing the contrast between the silicate band at $10 \mu m$, and the adjacent continuum, respect to opacity calculations considering only silicates. The silicate bands at $\sim 10 - 20 \mu m$ almost disappear from the total absorption coefficient for $a_{max} = 1$ mm (see also Figure 1), even for temperatures higher than the ice sublimation temperature. We find a similar result for $a_{max} \gtrsim 10 \mu m$ (in agreement with P94).

Figure 3 (upper panel) shows the mass absorption coefficient at $\lambda = 1.3$ mm as a function of maximum grain radius a_{max} for $p = 2.5$ and 3.5, and for a temperature $T < 100$ K. The opacity is almost constant for $a_{max} \leq 10 \mu m$, has a maximum around $a_{max} \sim 1$ mm and decreases for larger a_{max} as $\kappa_\nu \propto a_{max}^{3-p}$ for $3 < p < 4$ and $\kappa_\nu \propto a_{max}^{-1}$ for $p < 3$. This happens because the absorption coefficient at $\lambda \sim 1$ mm is dominated by grains with $a \sim 1$ mm and the mass of those grains is maximum for $a_{max} \sim 1$ mm and decreases for larger a_{max} , with a slope that depends on p . Our results agree closely with those of MN93, even though we use a different dust composition.

The straight line in Figure 3 (upper panel) is the opacity at 1.3 mm derived from the formula $\kappa_\nu = 0.1(\lambda/250 \mu m)^{-\beta}$, with $\beta = 1$ (BS91), commonly used to derive disk masses from mm-wave fluxes. At $\lambda = 1.3$ mm the value of this absorption coefficient is close to the maximum absorption coefficient, achieved when $a_{max} \sim 1$ mm, but is generally much larger for other grain sizes. In addition, according to P94, composite, unfilled grains have in general smaller opacities at 1 mm than compact spheres of the same size.

The frequency dependence of the dust opacity in the wavelength regime of interest, parameterized by $\beta = d \log \kappa_\nu / d \log \nu$, can in principle be used to constrain grain growth (BS91; MN93), depending on the chemical composition (P94). In Figure 3 (middle panel), we show the value of β in the mm-wave range,

$$\beta = \frac{\log(\kappa_{0.769mm}) - \log(\kappa_{1.3mm})}{\log(1.3mm) - \log(0.769mm)}, \quad (1)$$

as a function of maximum grain radius a_{max} for the same cases plotted in the upper panel. For

small grains ($a_{max} \leq 10 \mu\text{m}$), $\beta = \text{constant} \sim 1.75$, and approaches a maximum value for sizes $a_{max} \sim 60 - 300 \mu\text{m}$ (corresponding to $2\pi a/\lambda \sim 1$). The value of β decreases with increasing maximum size, and for $a_{max} > 10 \text{ cm}$, becomes independent of a_{max} . Our results are qualitatively consistent with those of MN93.

The detailed behavior of β for a_{max} between $100 \mu\text{m}$ and 1 cm depends on the relative importance of the different kind of grains. Small changes in abundances and optical properties can change the value of β in these intermediate sizes. In particular, according to P94, composite grains with 50 % void volume have a less steep increase of β with a_{max} , for grain sizes smaller than 1 mm .

Figure 3 (lower panel) shows that the albedo ω_ν at $\lambda = 1.3 \text{ mm}$ increases from 0 to ~ 0.9 for a_{max} between $10 \mu\text{m}$ and 1 cm (MN93). For larger values of a_{max} , $\omega_\nu \sim 0.9$ for $p=3.5$ and $\omega_\nu \sim 0.5$ for $p=2.5$. This large albedo means that scattered light contributions in the mm-wavelength range may not be neglected (MN93).

3. Disk Models

We solve self-consistently the complete set of vertical structure equations, including irradiation and viscous heating, resulting in detailed profiles of temperature and density with vertical height and disk radius. The assumptions, equations and method are described in Papers I and II. In particular, we assume that gas and dust are well mixed and in thermal balance everywhere. The input parameters to calculate the disk structure are the disk mass accretion rate \dot{M} , the viscosity parameter α , and the central star mass M_* , radius R_* and temperature T_* . Whenever it is possible, we use observational constraints to reduce the parameter space that must be explored. To this end we have chosen typical parameters of T Tauri stars from Gullbring et al. (1998): $\dot{M} = 3 \times 10^{-8} M_\odot \text{ yr}^{-1}$, $M_* = 0.5 M_\odot$, $R_* = 2 R_\odot$ and $T_* = 4000 \text{ K}$ for the fiducial model. We assume the disk is in steady state accretion, i.e. the accretion rate through the outer disk is the same as in the inner disk, at a rate inferred from measurement of the ultraviolet and optical continuum excess emission produced as material accretes via a shock at the stellar surface (Calvet and Gullbring 1998). The viscosity parameter α is changed appropriately to fix the disk mass. The adopted values of α are between 0.005 and 0.036, corresponding to disk masses between 0.1 and $0.02 M_\odot$ (for $\dot{M} = 3 \times 10^{-8} M_\odot \text{ yr}^{-1}$ and $R_d = 100 \text{ AU}$). The disk outer radius is taken to be $R_d = 50, 100$ and 200 AU , and the inner radius is $R_{hole} = 3 R_*$.

Given the disk structure, the emergent intensity is calculated by integrating the transfer equation,

$$I_\nu = I_\nu^{bg} e^{-\tau_{\nu,i}} + \int_0^{\tau_{\nu,i}} S_\nu(t_{\nu,i}) e^{-t_{\nu,i}} dt_{\nu,i} , \quad (2)$$

along rays that pierce the disk. Here, S_ν is the source function, $\tau_{\nu,i}$ is the total optical depth along a particular ray (with an inclination angle i respect to the symmetry axis of the disk), $t_{\nu,i}$ is the

variable optical depth along the ray, and I_ν^{bg} is the background radiation, i.e., $I_\nu^{bg} = B_\nu(T_{bg})$ with $T_{bg} = 2.73$ K. The optical depth is calculated including true absorptions and scattering events.

Since the dust albedo of large grains is so large in the mm range (Figure 3 and Table 1, it is important to include the contribution of the emissivity in scattered light. Assuming coherent and isotropic scattering, the source function is taken to be (Mihalas 1978)

$$S_\nu = (1 - \omega_\nu)B_\nu + \omega_\nu J_\nu , \quad (3)$$

where B_ν is the Planck function and J_ν is the mean intensity of the radiation field. We approximate the J_ν by the mean intensity of a vertically isothermal slab (see MN93), with the Planck function evaluated at the local temperature,

$$J_\nu(t_{\nu,0}) = B_\nu(t_{\nu,0}) \left\{ 1 + \frac{\exp[-\sqrt{3(1-\omega_\nu)} t_{\nu,0}] + \exp[\sqrt{3(1-\omega_\nu)} (t_{\nu,0} - \tau_{\nu,0})]}{\exp[-\sqrt{3(1-\omega_\nu)} \tau_{\nu,0}] (\sqrt{1-\omega_\nu} - 1) - (\sqrt{1-\omega_\nu} + 1)} \right\} , \quad (4)$$

where $\tau_{\nu,0}$ is the total optical depth in the vertical direction ($i = 0^\circ$) and $t_{\nu,0}$ is the variable optical depth in the same direction.

In an attempt to simulate the observational procedure of taking on-off measurements, the background intensity I_{bg} due to the cosmic microwave background is subtracted from the disk emergent intensity given by equation (2). The observed flux is calculated by integrating the intensity, emerging in a direction defined by the line of sight, over the solid angle subtended by the disk as seen by the observer. For optically thin regions, the emergent flux calculated including scattering is similar to the flux calculated assuming the dust is purely absorbing. For optically thick regions, with $\tau_{\nu,0} \gg 1/(1 - \omega_\nu)$, the flux for a pole-on disk is smaller by a factor roughly $1 - \omega_\nu / [\sqrt{1 - \omega_\nu} + 1][\sqrt{3(1 - \omega_\nu)} + 1]$ than the purely absorbing case, consistent with the discussion in MN93. For intermediate optical depths (e.g. $\tau_{\nu,0} \sim 1$), the behavior of the emergent flux cannot be described by analytic expressions.

4. Results

4.1. Disk “photosphere” and hidden central stars

Figure 1 shows that grain growth affects the opacity at both small and large wavelengths. For a fixed mass of dust, increasing a_{max} tends to increase the mm-wave opacity (for $a_{max} \lesssim mm$) at the same time as it decreases the opacity at the characteristic wavelength of the stellar radiation, $\lambda \sim 1 \mu m$. This has important effects on the disk temperature distribution and thus the disk structure.

Figures 4 and 5 show the midplane temperature T_c , surface density Σ and the height of the “irradiation surface” z_s as a function of radius, and the SEDs of pole-on ($i = 0^\circ$) disks, for different grain size distributions and the same disk mass $M_d \approx 0.046 M_\odot$, accretion rate

$\dot{M} = 3 \times 10^{-8} M_{\odot} \text{yr}^{-1}$ and the typical central star properties mentioned in §3. The height z_s is defined to be where the mean optical depth to the stellar radiation is unity (using the mean opacity χ_P^* , listed in Table 1) and represents where most of the stellar radiative energy is deposited (see paper II). The height of this surface decreases when the grain sizes increases. Thus, the fraction of stellar radiation intercepted by the disk decreases, resulting in a colder disk than what would be expected for smaller grains. The mass surface density of the outer disk is $\Sigma \sim 1/R$ for $R > 10$ AU, thus the disk mass is dominated by the contribution of the outer radii. Since the present models have all the same disk mass, they also have the same surface density for $R \gtrsim 10$ AU.

In Paper II we showed that if the disk has ISM-dust well-mixed with the gas, then a large fraction of the CTTS should have their central star extinguished with $A_V > 30$ mag (30 % of all objects with an outer disk radius $R_d = 100$ AU). Also, the two-layer models of Chiang & Goldreich (1997,1998) implies a similar large fraction of highly-extinguished central stars. As discussed in Paper II, this fraction is too high in comparison with estimates from current observational surveys in the Taurus molecular cloud complex. The decrease in the optical and near-infrared dust opacity with increasing a_{max} results in (optically and geometrically) thinner disks, and thus the fraction of highly-extinguished stars predicted for a random distribution of viewing inclinations decreases. Figure 6 shows the cosine of the critical angle i_c , such that $\cos i_c = \mu_c = z_{A_V}(R)/[z_{A_V}(R)^2 + R^2]^{1/2}$, where $z_{A_V}(R)$ is the height at which the the extinction coefficient is $A_V = 30$. Assuming a random distribution of disk rotation axes to the line of sight, for $a_{max} = 1$ mm and $p = 3.5$, 20 % of the T Tauri stars with disks with a typical radius $R_d \sim 100$ AU, should be extinguished by their disks with an $A_V > 30$ mag, while for $a_{max} = 10$ cm and $p = 2.5$ only ~ 6 % of T Tauri should have $A_V > 30$ mag. Because the fraction of such disk-obscured sources in Taurus is estimated to be not more than about 15 % (Paper II), it is clear that the grain-growth models are in much better agreement with the current observational constraints.

The SEDs of the models show that the larger the fraction of big grains, the smaller the mid- and far-IR fluxes. On the other hand, the mm fluxes increases with a_{max} until $a_{max} \sim 1$ mm, and decreases with a_{max} for larger grains, reflecting the behavior of the opacity shown in Figure 3. In the next section we show how the SED of a disk model with a larger fraction of big grains than the ISM dust compare to observations.

4.2. Median SED

Figure 7 shows the spectral energy distributions (SEDs) for two disk models, both with $M_d = 0.046 M_{\odot}$ ($\dot{M} = 3 \times 10^{-8} M_{\odot} \text{yr}^{-1}$, $\alpha = 0.01$, $R_d = 100$ AU) and a central star with $M_* = 0.5 M_{\odot}$, $R_* = 2 R_{\odot}$ and $T_* = 4000$ K ($L_* = 0.9 L_{\odot}$), and an inclination angle $\cos i = 0.65$ ⁴.

⁴We use $\cos i = 0.65$ instead of 0.5 for the average inclination to account for the occultation in edge-on systems, which would drop out of the observational samples due to weak optical and infrared emission.

We adopt the distance to Taurus of 140 pc (Kenyon, Dobrzycka and Hartmann 1994). One of the models has ISM-dust and the second model has dust with the abundances and optical properties described in §2, and $a_{max} = 1$ mm, $p = 3.5$. The main difference between both models are that the ISM-dust disk model has larger far-IR and smaller mm-wave fluxes than the grain growth model. Both models are compared to the median SED for the T Tauri stars in the Taurus-Auriga molecular cloud (from Kenyon & Hartmann 1995, c.f., Paper II). The SED for the $a_{max} = 1$ mm disk model is much closer to the observed median spectrum. A range of values of a_{max} and $p = 2.5 - 3.5$ produce SEDs consistent with the quartiles (c.f. Figures 4 and 5). Also, disks must have different radii, inclination angles, environment, etc., which would contribute to the scatter in the observed SEDs (c.f., paper II).

4.3. Scattered light images

The decrease in opacity at small wavelengths when the fraction of large grains increases also affects images in stellar scattered light. Figure 8 shows images in scattered light of edge-on disk models ($i = 90^\circ$), with the typical properties described in §3 and a viscosity parameter $\alpha = 0.01$. These disk models have $R_d = 100$ AU and $M_d = 0.046 M_\odot$, and again are assumed to lie at a distance of 140 pc. The images are calculated at $\lambda = 0.814 \mu m$, in the single scattering approximation, assuming a Henyey-Greenstein phase function, with an asymmetry parameter $g = 0.65$. The emergent intensity distribution has been convolved with the HST PSF (for the filter F814W/PC1). The aspect ratio of the image, i.e. the width of the central dark lane or equivalently the distance between emission maxima, is very sensitive to a_{max} for a given p . In this case, the larger the value of a_{max} the smaller the width of the dark lane, which almost disappears for $p = 2.5$, $a_{max} = 10$ cm. This occurs because the opacity at $\lambda \sim 0.8 \mu m$ decreases when a_{max} increases and p decreases (c.f §2 and Table 1), and both the height of the surface where the stellar radiation is attenuated (c.f §4.1) and the extinction of the scattered light at a given height produced by the outer disk decrease. For the same reason, the maximum intensity of the images increases with a_{max} . The width of the dark lane also depends on the outer disk radius. The height where most of the stellar radiation is deposited (z_s , c.f. Figures 4 and 5) evaluated at the the disk radius can be used to make a rough prediction of the distance between the emission peaks. It is not very sensitive to the disk inclination, as long as the the disk occults the central star.

In Paper II we showed that the near-IR scattered light image predicted for the well-mixed ISM-dust models produces an aspect ratio ~ 2 times larger than is consistent with *Hubble Space Telescope* images of HK Tau/c and HH 30. The results shown in figure 8 show that grain growth will improve the comparison between theory and observation. Here we consider a detailed comparison between the the image of HK Tau/c and a disk model.

Figure 9 shows the image of a disk model with $\dot{M} = 3 \times 10^{-8}$, $\alpha = 0.01$, $T_* = 3500$ K, $R_* = 1.3 R_\odot$ ($L_* = 0.22 L_\odot$), $M_* = 0.5 M_\odot$, $R_d = 110$ AU, inclination angle $i = 89.8^\circ$ and position angle P.A. = 40° . The disk model dust is characterized by $a_{max} = 1$ m and $p = 3.5$, and the total

opacity and albedo are given in Table 1.

The model image is compared to the image of HK Tau/c (Stapelfeldt et al. 1998), with the same contour levels in both images as in Figure 8. The observed image and the model show reasonable agreement, as for instance the distance between maxima, the aspect ratio and the maximum brightness. The flux at $\lambda = 1.3$ mm predicted by this model is $F_{1.3\text{ mm}} = 8$ mJy, consistently smaller than the flux for the unresolved HK Tau binary system reported by Beckwith et al. (1990) (= BSCG), $F_{1.3\text{ mm}} = 41$ mJy. The mass of this disk model is $M_d = 0.065 M_\odot$. We find that growth to a very large value of a_{max} yields a dramatically reduced mm-wave opacity, and thus a very low mm-wave flux for this large disk mass (see §5), while producing an optical image in good agreement with observations.

On the other hand, dust grains with $a_{max} = 1$ mm and $p = 2.5$ have, approximately, the same opacity and albedo at $\lambda = 0.8 \mu m$, but a much larger opacity at 1.3 mm (c.f., Table 1). We made a disk model with the same mass and central star properties than the one shown in Figure 9 and we found it has a similar scattered light image, but a much larger flux at 1.3 mm, $F_{1.3mm} \sim 30$ mJy. However, this flux seems too high, considering that the total flux should have contributions from both disks in the binary, and that the less inclined disk of the primary is expected to have a larger contribution.

The model shown in Figure 9 is not unique, being under-constrained by observations. Nonetheless, this example illustrates how disk masses inferred from optical imaging (or even mm-wave fluxes) may be substantially under-estimated. Without additional observational constraints on dust properties, detailed conclusions are difficult to derive.

Moreover, the mass of the present model is several hundred times larger than the mass inferred by Stapelfeldt et al. (1998) (i.e., their models C and D have masses $M_d \sim 5.9 \times 10^{-5} - 1.2 \times 10^{-4} M_\odot$). The discrepancy is due to the difference in dust opacity. Stapelfeldt et al. used an opacity typical of ISM dust grains, which is much larger at $\lambda = 0.8 \mu m$ than the opacity corresponding to a larger value of a_{max} (see Table 1). This implies that they require a much smaller disk mass than we do to reproduce the width of the dark lane of the image and its aspect ratio. Assuming that the disk is optically thin and the flux at 1.3 mm scales with disk mass and the absorption coefficient, using the values given in Table 1 we infer $F_{1.3mm} \sim 0.01$ mJy for their model D. Thus, mm observations resolving the binary system would be very important to define whether this is a very low-mass disk with ISM type of dust or a moderate mass disk with a much smaller fraction of small grains than the ISM dust, as we suggest here.

5. Disk mm-wave fluxes and masses

Much of what is known or estimated about T Tauri disks comes from analyses of mm- and sub-mm wavelength emission. The first observational arguments in support of grain growth were made to explain observed spectral indices in this wavelength regime (BSCG, BS91). Our previous

models (Paper II) with ISM-dust could not explain the observed mm-wave fluxes. In this section we discuss our detailed model results for disks with larger grains in this wavelength region.

In principle, disk masses and aspects of grain properties can be derived from long-wavelength fluxes and spectral slopes. The analysis is particularly easy when the disk is optically thin. In this case the observed flux is proportional to the disk mass, absorption coefficient at the wavelength of observation, and the source function at this wavelength. At long wavelengths the source function is expected to have a Rayleigh-Jeans wavelength or frequency dependence, so that the flux is then $F_\nu \propto M_d k \langle T \rangle / c^2 \nu^2 \kappa_\nu$, where k is the Boltzmann constant, c is the speed of light, and $\langle T \rangle$ is a mass-weighted disk mean temperature. The spectral index $d \log F_\nu / d \log \nu$ is the product of the intrinsic dependence of the dust opacity times the Rayleigh-Jeans distribution. Unfortunately, optical depth effects cannot be ignored in general and the source function may not have a Rayleigh-Jeans form if the dust temperature is too low (BS91), so in general detailed models must be used to compare with observations.

To make this comparison we constructed model sequences of fixed disk mass with differing dust properties. The stellar luminosity, stellar mass, and radius are fixed as before at $0.9 L_\odot$, $0.5 M_\odot$ and $2 R_\odot$ (c.f., §3). We assumed a fixed mass accretion rate $\dot{M} = 3 \times 10^{-8} M_\odot \text{ yr}^{-1}$ and a fixed outer radius of $R_d = 100 \text{ AU}$ in our basic sequence. Changing the disk mass in our models then requires us to change the α parameter accordingly. Since the viscous heating in the outer disk in the basic sequence is small, so that the temperature distribution is controlled by irradiation, this is roughly equivalent to adopting a constant viscosity parameter and varying \dot{M} instead to change the disk mass. The disk masses in each sequence are $M_d = 0.023 M_\odot$, $0.046 M_\odot$, and $0.092 M_\odot$. We assume initially that the disks are viewed pole-on, and discuss the effects of changing the inclination angle later.

Figure 10 shows the 1.3 mm flux vs. n for several sequences of disk models of fixed mass (connected points) The spectral index n is given by

$$n = \frac{\log(F_{0.769\text{mm}}) - \log(F_{1.3\text{mm}})}{\log(1.3\text{mm}) - \log(0.769\text{mm})}. \quad (5)$$

Each point along a given sequence corresponds to a different value of a_{max} (between $10 \mu\text{m}$ and 1 cm); the two panels correspond to $p = 3.5$ (upper) and $p = 2.5$ (lower).

We discuss the model sequences beginning on the right-hand side of the figure, where the models have small a_{max} , and moving counter-clockwise along the curves as a_{max} increases. For small a_{max} , the spectral index is relatively large, reflecting the intrinsic wavelength dependence of the dust opacity, though the actual value of n departs from the Rayleigh-Jeans limit $2 + \beta \sim 3.75$ because this limit is not applicable in this wavelength range for the low temperatures ($\sim 10 - 20 \text{ K}$) characteristic of the outer disk. The flux levels scale nearly linearly with the mass, as expected in the optically-thin case; only the inner, high-surface density regions are optically thick, and these regions do not contain much mass. Proceeding to larger a_{max} , the spectral index decreases, both because larger regions of the disk become optically thick due to the increase in opacity (Figure 3)

and because of the decrease in β , which affects the frequency dependence of the emission from the optically thin regions (cf. Figure 3). As a consequence of the grain albedo, the total optical depth of the disk has to be $\tau_0 \gtrsim 1/(1-w)^{1/2}$ for the emergent flux to approach the optically thick limit for pure thermal emission. For the models plotted in Figure 10, this limit is reached only by the most massive disk ($M_d \sim 0.1 M_\odot$) when $a_{max} = 1$ mm. Finally, for much larger a_{max} , the disk models become mostly optically thin, and so the fluxes and spectral indexes much more closely reflect the dust opacity and disk mass. The $p = 2.5$ models show much more variation in n at large dust sizes because β changes more rapidly with increasing a_{max} than in the $p = 3.5$ case (Figure 3). For reference we also show the flux and spectral index of disk models with the same masses calculated assuming they contain ISM-dust (large open triangles). In this case the outer disks are optically thin, and the opacity is too small to account for the observed fluxes.

To compare with our models we show observations of Taurus stars taken from BSCG and BS91 as stars in Figure 10. The observed spectral index is calculated as $n = \beta_p + 2$, where β_p , taken from Beckwith & Sargent (1991), is the result of power law fits to the spectral energy distributions between 1.3 mm and either 0.624 mm or 0.769 mm. We ignore the effects of the different wavelength limits on the spectral index; this has little effect on the comparison, given the typical errors shown by the error bar in Figure 10 (BS91). Figure 10 shows that the disk models generally span the range of observed fluxes and spectral indexes larger or similar to $n \sim 2$.

Figure 10 also shows the flux and spectral index of flat irradiated disk models, with $a_{max} = 1$ mm. Here we have assumed that the disks are geometrically flat, which corresponds to complete dust settling to the disk midplane. These disks are much colder at a given radius than those in which dust and gas are well mixed up to several scale heights (flared disks), since they intercept a smaller fraction of the stellar radiation (e.g., Hartmann 1998). The emission of these flat disks is dominated by optically thick and cold regions and both the flux and the spectral index are smaller ($n < 2$) than in the flared models. Thus, the CTTS with $n < 2$ and a larger mm flux than the flat disk models could be intermediate cases, in which just a fraction of dust has been settled towards the midplane.

Panel (a) in figure 11 shows the effect of changing the outer disk radius. We have selected the parameters (i.e., \dot{M} and α) of the model with intermediate mass in Figure 10. The models have $R_d = 50$ AU (dashed line), $R_d = 100$ AU (solid line) and $R_d = 200$ AU (dotted line), corresponding to masses $M_d \approx 0.02, 0.05$ and $0.092 M_\odot$, respectively (similar to the disk masses represented in Figure 10). In general, the flux scales as $\sim R_d^{1/2}$, as expected for an optically thin disk with $I_\nu \sim B_\nu \tau_\nu \propto R^{-3/2}$. However, for $a_{max} \sim 1$ mm and $R_d = 50$ AU, a larger fraction of the disk becomes optically thick which is reflected by $n \rightarrow 2$.

Panel (b) in figure 11 shows the effect of changing inclination angle. For the same model with intermediate mass and a radius $R_d = 100$ AU ($M_d \sim 0.046 M_\odot$), we change the inclination angle $\cos i = 0.25$ (dashed), 0.5 (solid) and 0.9 (dotted). For $a_{max} < 150 \mu m$, the fluxes are similar reflecting that the disk is mainly optically thin at $\lambda = 1.3$ mm, but the spectral index tends to

decrease with the inclination of the disk, because the relative contribution of the optically thick inner regions changes at both wavelengths. For $a_{max} > 1$ mm, the flux roughly scales with $\cos i$, and the spectral index is almost constant $n \sim 2.4$.

Panel (c) in figure 11 shows the flux vs spectral index of pole-on disk models with different mass accretion rates and masses, assuming no irradiation by the central star, i.e. the disk heating is entirely due to viscous dissipation (Paper II). Each connected sequence corresponds to disk masses of $M_d = 0.023, 0.046$ and $0.092 M_\odot$ and each point along a sequence corresponds to a different mass accretion rate (roughly differing by a factor 3). We take $a_{max} = 1$ mm and $p = 3.5$ for all models. The flux increases with temperature (or \dot{M}) and the spectral index is sensitive to both the disk temperature and mass. In these models the outer disk is very cold ($T \sim 5 - 15$ K)⁵ and the Rayleigh-Jeans limit is not valid. Unfortunately, since the optical depth is close to unity, one cannot use neither the optically thin nor the optically thick limits of equation (4) to approximate the mm-wave fluxes emerging from the disk by simple expressions. In addition, the disk temperatures are comparable to the cosmic background temperature and the optical depth of the disk is large, so the correction introduced when we subtract $B_\nu(T_{bg})$ to the emergent intensity of the disk (c.f. §3) becomes very important. Besides this complications in describing analytically the results shown in Figure 11, the conclusions are simple. Larger mass accretion rates for these pure viscous disk models result in larger mm-wave fluxes. On the other hand, the smaller the disk mass, the smaller the flux and the larger the spectral index, because the smaller the optical depth. These models have $1 \lesssim n \lesssim 2.6$, but require large mass accretion rates and small inclination angles to have mm-wave fluxes consistent with the observations.

Panel (d) shows the same models as in panel (c), but including irradiation from the central star. All the models with different mass accretion rates at a given mass have almost the same flux at 1.3 mm and the same spectral index, because the stellar irradiation is the dominant heating source of the outer disk ($R \gtrsim 20$ AU).

6. Discussion

We have shown that self-consistent disk models with power-law distributions of grains, with $p \sim 2.5 - 3.5$, and maximum sizes $a_{max} \sim 1$ mm, can reproduce many general features of observed T Tauri disks, including SEDs, optical and near-infrared images, limits on the frequency of disk-obscured systems, and mm-wavelength fluxes and spectral indexes. In contrast, our results of Paper II showed that ISM dust properties were not in good agreement with observations. Our findings reinforce previous suggestions (e.g., BS91, MN93) for grain growth in T Tauri disks with typical ages of 1 Myr. We make these suggestions stronger, however, since we aim to fulfill more

⁵We include the disk heating by cosmic rays and radioactive decay of ^{26}Al , but the disk is so dense that it cools efficiently, and can reach temperatures lower than 10 K.

observational constraints.

The inference of substantial grain growth implies that there must be significant uncertainties in deriving disk properties such as masses. If dust agglomeration has proceeded from typical interstellar sizes of $0.1 \mu\text{m}$ to a 1 mm or larger, there is no particular reason to assume that growth has proceeded to precisely the same value of a_{max} in all systems. While it may be possible to argue that a_{max} is at least $\sim 1 \text{ mm}$ on the basis of observed spectral indexes (Figure 8), it is difficult to eliminate the possibility of growth beyond this size from n alone because β approaches a constant for larger a_{max} (Figure 3). This uncertainty in dust size distributions (even assuming p can be constrained to lie between $\sim 2.5 - 3.5$) results in a corresponding uncertainty in disk masses and other properties.

Limiting dust opacity variations by constraining a_{max} to lie between $100 \mu\text{m}$ and 1 cm , our disk models suggest that disk masses between $\sim 10^{-2}M_{\odot}$ and $\sim 10^{-1}M_{\odot}$ are consistent with the data. The upper end of this mass range encompasses disks subject to gravitational instability. Specifically, the Toomre parameter Q (e.g., D’Alessio et al. 1999b) at $R_d = 100 \text{ AU}$ is $Q \sim 1$ for the $M_d = 0.05M_{\odot}$ models and $Q \sim 0.5$ in the $M_d = 0.1M_{\odot}$ models, suggesting that the former model is close to instability and the latter is strongly unstable. Thus, the possibility of gravitational instabilities in at least some T Tauri disks cannot be dismissed. In this regard, models shown in panels (c) and (d) of Figure 11 indicate that observed high mm fluxes and low spectral indices of some of the stars could be explained by high mass disks with high mass accretion rates, as long as their outer disks were not heated by irradiation. Interestingly, some of the stars with $n < 2$ (CW Tau, DR Tau and DL Tau) are high mass accretion rate stars with $\dot{M} \sim 2 \times 10^{-7} - 8 \times 10^{-6} M_{\odot} \text{ yr}^{-1}$ (Hartigan, Edwards & Ghandour 1995). We may speculate that one possible interpretation is that these disks may be gravitationally unstable and the outer disks are shadowed from the star by density perturbations produced by the development of the instability, as models suggest (e.g., Pickett et al. 2000, Nelson et al. 2000). If one assumes that the disk masses are always smaller than the gravitational stability limit, then the high mm fluxes shown in Figure 10 cannot be understood if grains have grown beyond about 1 cm in size. However, growth to larger sizes could be accommodated in the inner disk; these are optically thick regions and the resulting emission is insensitive to their total mass.

The models predict that less-luminous disks are more likely to be optically thin and thus exhibit spectral indexes which reflect the intrinsic wavelength dependence of the dust opacity much more closely. There are many nearby T Tauri stars whose 1.3 mm fluxes lie in the range of $\sim 15 - 30 \text{ mJy}$ (Osterloh & Beckwith 1995) for which mm-wave spectral indexes have not been published. Observations of spectral indexes for these fainter objects could more clearly demonstrate particle growth. However, because the spectral index tends to a limiting value when a_{max} becomes large, it will be difficult to tell whether low mm-wave emission is due to low intrinsic disk mass or particle growth, unless mid- and far-IR fluxes and scattered light images are used to disentangle disk mass and grain sizes.

In principle, geometrically-thinner disks could be the result of dust settling alone. However, our analysis of the mm-wave fluxes and spectral indexes indicates that grain growth is essential. Because the growth of particles reduces the opacity at short wavelengths, it is difficult to distinguish between the effects of settling and grain growth on observed SEDs and images. The case of HK Tau/c illustrates how one may arrive at very different conclusions about disk masses depending upon the dust properties assumed.

Of course, grain growth should be accompanied by settling; larger particles tend to fall more rapidly toward the disk midplane (e.g., Weidenschilling & Cuzzi 1993, Weidenschilling 1997). Miyake & Nakagawa (1995) argue that settling has to occur in some T Tauri disks on the basis of their infrared SEDs. Two of our results also support the idea of settling. First, our models generally cannot explain the T Tauri stars with moderately low mm-wave fluxes and small values of n (e.g., Figure 10). Flat disks produce lower mm-wave fluxes and smaller spectral indexes, because the reduced irradiation fluxes reduce the outer disk temperatures. Our detailed calculations show that geometrically-flat disks result in too small values of flux and n , but the results shown in Figure Figure 10 suggest that disks with intermediate thicknesses (i.e., some settling of dust) could explain the T Tauri disks found in the lower-left hand region of the flux-spectral index diagram.

Second, our models with $a_{max} \sim 1$ mm and $p = 2.5 - 3.5$ have no silicate feature, in contrast with observations of many T Tauri stars (Cohen and Witteborn (1985), Natta, Meyer & Beckwith 2000). In the context of our disk models, in which the relative grain size distribution is independent of height and radius, putting more of the total dust mass into large grains (grain growth) reduces the geometrical disk thickness at large radii, in better agreement with observations, but results in too few small grains at 1 AU ($T \sim 100$ -300 K) to produce 10μ silicate emission. We could improve the agreement with observations by having more small grains at 1 AU than at large radii. If the grain size distribution is independent of height, this would imply that there has been less grain growth at small radii than at large disk radii. It seems much more likely that there has been faster grain growth at small radii, but that the large grains have also settled more toward the midplane in the inner disk. This settling could result in a much larger fraction of small grains in the upper atmospheric layers at 1 AU, which is the region where the silicate emission is formed (Calvet et al. 1992; Chiang & Goldreich 1997).

It is therefore clear that improved disk models for T Tauri stars will have to incorporate both grain growth and settling in a physically self-consistent manner, accounting for the radial and vertical dependences of both process. We will develop such models in a forthcoming paper.

This work was supported in part by the Visiting Scientist Program of the Smithsonian Institution, by NASA grant NAG5-9670, by Academia Mexicana de Ciencia and Fundación México-EEUU para la Ciencia, by CONACyT grant J27748E, México. We thank Luis Felipe Rodríguez for important advice about observational procedures in the mm-wave range, Karl Stapelfeld for sending us the image of HK Tau/c, Mordecai Mark Mac Low and Javier Ballesteros for useful discussions during this work. We also thanks Robbins Bell for a prompt and useful

referee report. PD acknowledges the hospitality of the Astrophysics Department of Columbia University and a fellowship of DGAPA-UNAM, México.

REFERENCES

- Beckwith, S.V.W., Sargent, A.I., Chini, R. S., & Guesten, R. 1990, *AJ*, 99, 1024 (BSCG)
- Beckwith, S.V.W., & Sargent, A.I. 1991 *ApJ*, 381, 250 (BS91)
- Beckwith, S. V. W., Henning, T. & Nakagawa, Y., 2000, in *Protostars and Planets IV*, (Tucson: University of Arizona Press), eds Mannings, V., Boss, A.P., Russell, S. S, p. 533
- Begemann, B., Dorschner, J., Henning, T., Mutschke, H., & Thamm, E. 1994, *ApJ*, 423, 71
- Calvet, N., Patiño, A., Magris, G., & D'Alessio, P. 1991, *ApJ*, 380, 617 (CPMD).
- Calvet, N., Magris, G., Patiño, A., & D'Alessio, P. 1992, *Rev. Mex. Astronom. Astrofís.*, 24, 27
- Calvet, N. and Gullbring, E. 1998, *ApJ*, 509, 802
- Campbell, M. J. & Ulrichs, J., 1969, *J. Geophys. Res.*, vol. 74, p. 5867
- Chiang, E.I., & Goldreich, P., 1997 *ApJ*, 490, 368 (CG)
- Chiang, E. I. and Goldreich, P. 1999, *ApJ*, 519, 279
- Cohen, M. and Witteborn, F. C. 1985, *ApJ*, 294, 345
- D'Alessio, P. 1996, Ph.D. Thesis, Universidad Nacional Autónoma de México, México
- D'Alessio, P., Cantó, J., Calvet, N., & Lizano, S. 1998, *ApJ*, 500, 411 (DCCL) (Paper I)
- D'Alessio, P., Cantó, J., Hartmann, L., Calvet, N. and Lizano, S. 1999, *ApJ*, 511, 896
- D'Alessio, P., Calvet, N., Hartmann, L., Lizano, S. and Cantó, J. 1999, *ApJ*, 527, 893 (Paper II)
- Draine, B. T., & Lee, H. M. 1984, *ApJ*, 285,89
- Gullbring, E., Hartmann, L., Briceño, C, & Calvet, N. 1998, *ApJ*, 492, 323
- Hartigan, P., Edwards, S., & Ghandour, L. 1995, *ApJ*, 452, 736
- Hartmann, L. 1998, *Accretion processes in star formation / Lee Hartmann*. Cambridge, UK ; New York : Cambridge University Press, 1998. (Cambridge astrophysics series ; 32) ISBN 0521435072.,
- Hartmann, L., Calvet, N., Gullbring, E., & D'Alessio, P. 1998, *ApJ*, 495, 385
- Henning, T. & Stognienko, R., 1996, *A&A*, 311, 291
- Henning, Th., Il'In, V. B., Krivova, N. A., Michel, B., & Voshchinnikov, N. V. 1999, *A&AS*, 136, 405

- Kenyon, S.J., & Hartmann, L. 1987, *ApJ*, 323, 714 (KH87)
- Kenyon, S. J., Dobrzycka, D. and Hartmann, L. 1994, *AJ*, 108, 1872
- Kenyon, S.J.,& Hartmann, L. 1995, *ApJS*, 101,117 (KH95)
- Laor, A. & Draine, B. T., 1993, *ApJ*, 402, 441
- Mannings, V. & Emerson, J. P. 1994, *MNRAS*, 267, 361
- Meakin, P., & Donn, B., 1988, *ApJ*, 329, L39
- Mihalas, D. 1978, *Stellar Atmospheres* (San Francisco:Freeman)
- Miyake, K., & Nakagawa, Y. 1993, *Icarus*, 106, 20 (MN93)
- Miyake, K., & Nakagawa, Y. 1995, *ApJ*, 441, 361
- Natta, A., Meyer, M.R., Beckwith, S.V.W. 2000, *ApJ*,534, 838
- Nelson, A. F., Benz, W. and Ruzmaikina, T. V. 2000, *ApJ*, 529, 357
- Osterloh, M., & Beckwith, S.V.W. 1995, *A&A*, 295, 31
- Pickett, B. K., Durisen, R. H., Cassen, P. and Mejia, A. C. 2000, *ApJ*, 540, L95
- Pollack, J. B., Hollenbach, D., Beckwith, S., Simonelli, D. P., Roush, T. & Fong, W. 1994, *ApJ*, 421, 615 (P94)
- Stapelfeldt, K.R., Krist, J.E., Ménard, F., Bouvier, J., Padgett, D.L., & Burrows, C.J. 1998, *ApJ*, 502, L65
- Warren, S.G., 1984, *Applied Optics*, vol. 23, p. 1206.
- Weidenschilling, S.J. & Cuzzi, J.N. 1993, in *Protostars and Planets III*, eds. E.H. Levy & J.I. Lunine (Tucson: University of Arizona Press), p. 1031
- Weidenschilling, S.J. 1997, *Icarus*, 127, 290
- Weingartner, J. C. & Draine, B. T., 2000, in preparation
- Wiscombe, W.J., 1979, *Mie scattering calculations: advances in technique and fast, vector-speed computer codes*, NCAR/TN-140 + STR, National Center for Atmospheric Research, Boulder, Colo.

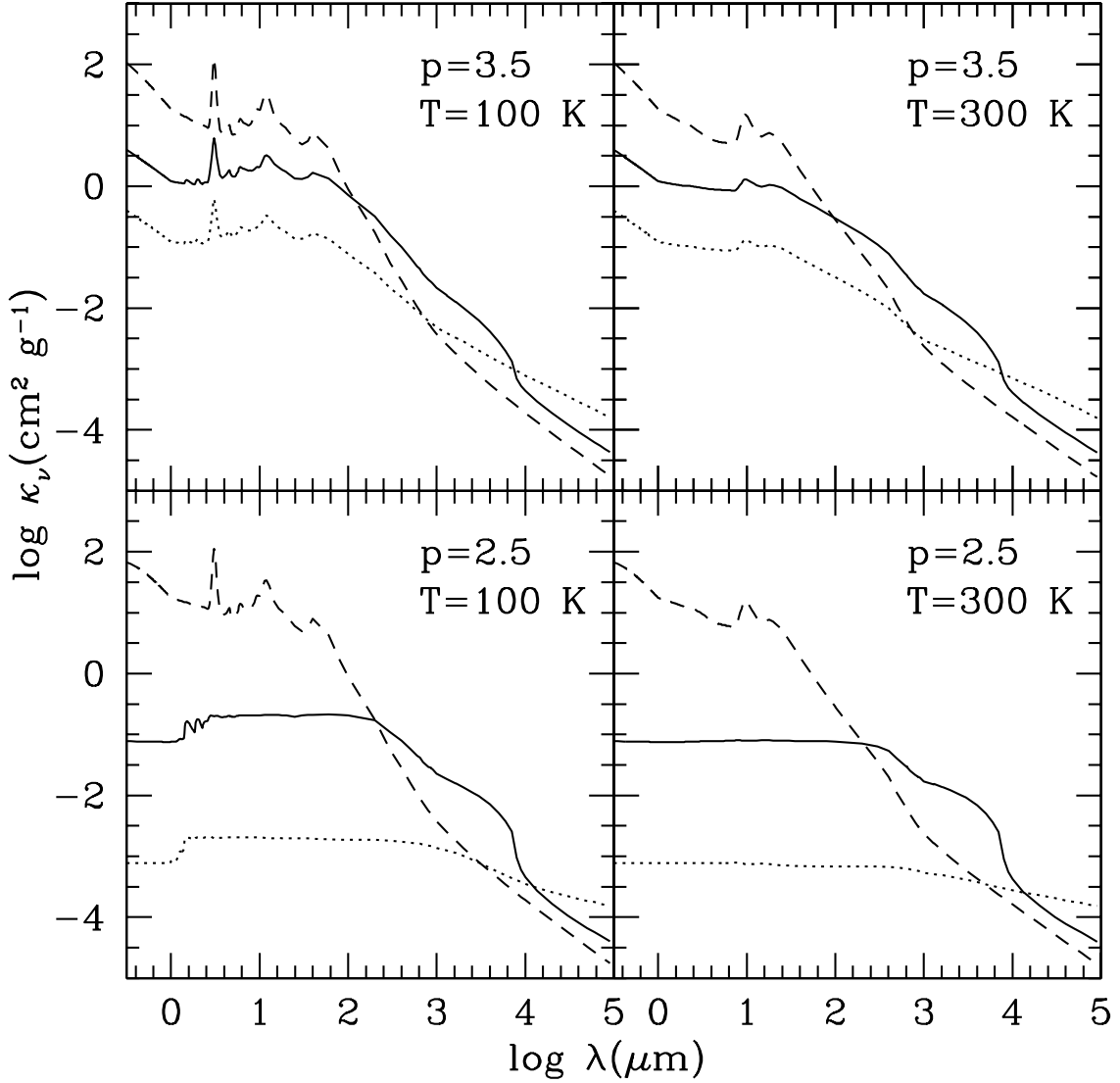


Fig. 1.— Mass absorption coefficient κ_ν vs wavelength for a grain size distribution characterized by $p = 3.5$ (upper panels) and 2.5 (lower panels). Each curve corresponds to a different grain maximum size: $a_{max} = 1 \mu m$ (dashed line), $1 mm$ (solid line), $10 cm$ (dotted line). The absorption coefficient is shown for $T = 100 K$ (i.e., all the different kind of grains are present) and $T = 300 K$ (i.e., water ice has been sublimated). Each panel is labeled by p and T .

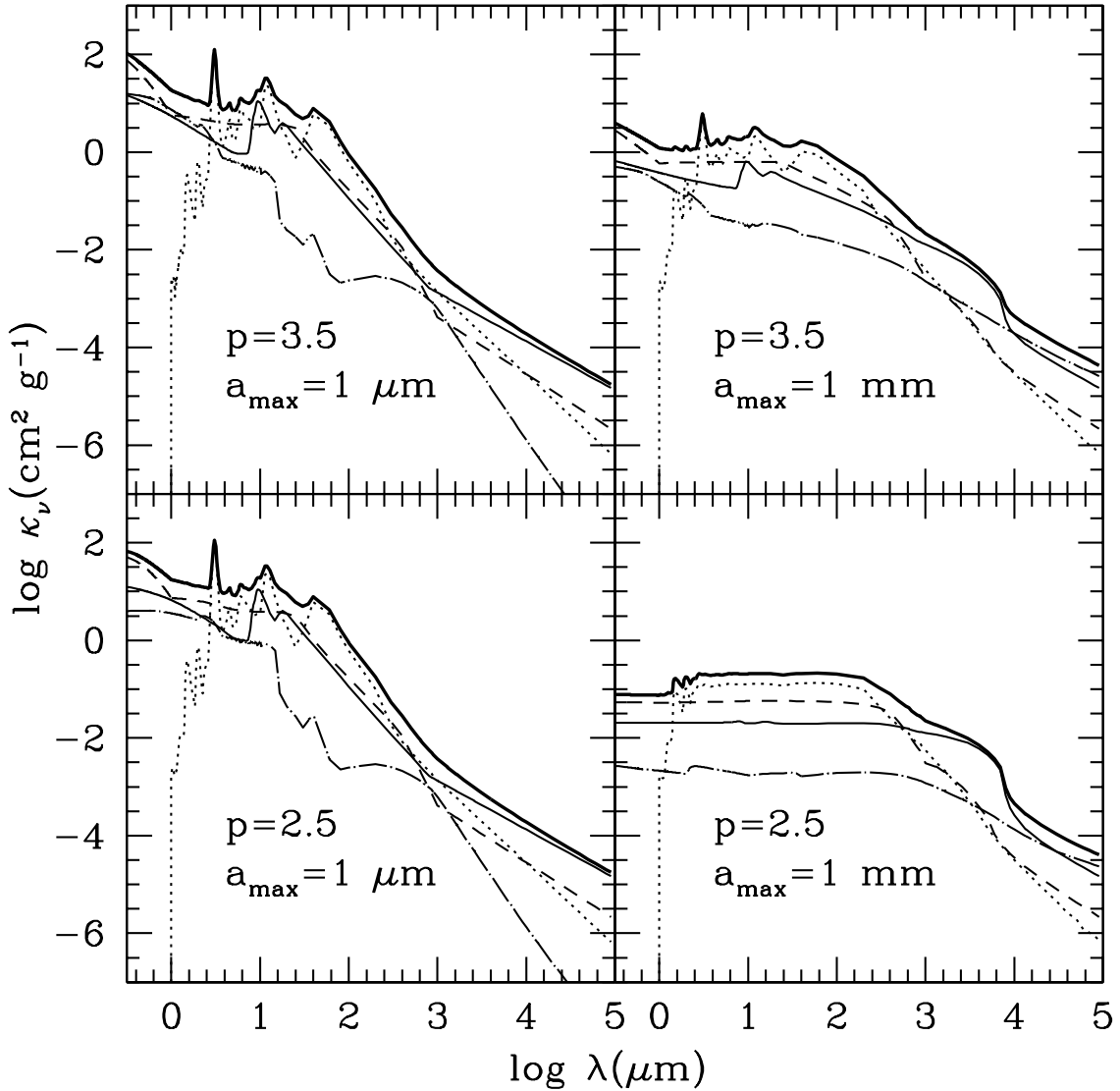


Fig. 2.— Mass absorption coefficient κ_ν vs wavelength for a grain size distribution characterized by $p = 3.5$ (upper panels) and $p = 2.5$ (lower panels), with $a_{\max} = 1 \mu\text{m}$ (left panels) and 1 mm (right panels), for a temperature $T = 100 \text{ K}$. Each curve corresponds to a different kind of grain: silicates (light solid line), water ice (dotted line), organics (dashed line), troilite (dot-dashed line). The total mass absorption coefficient is represented with a solid thick line. Each panel is labeled by p and a_{\max} .

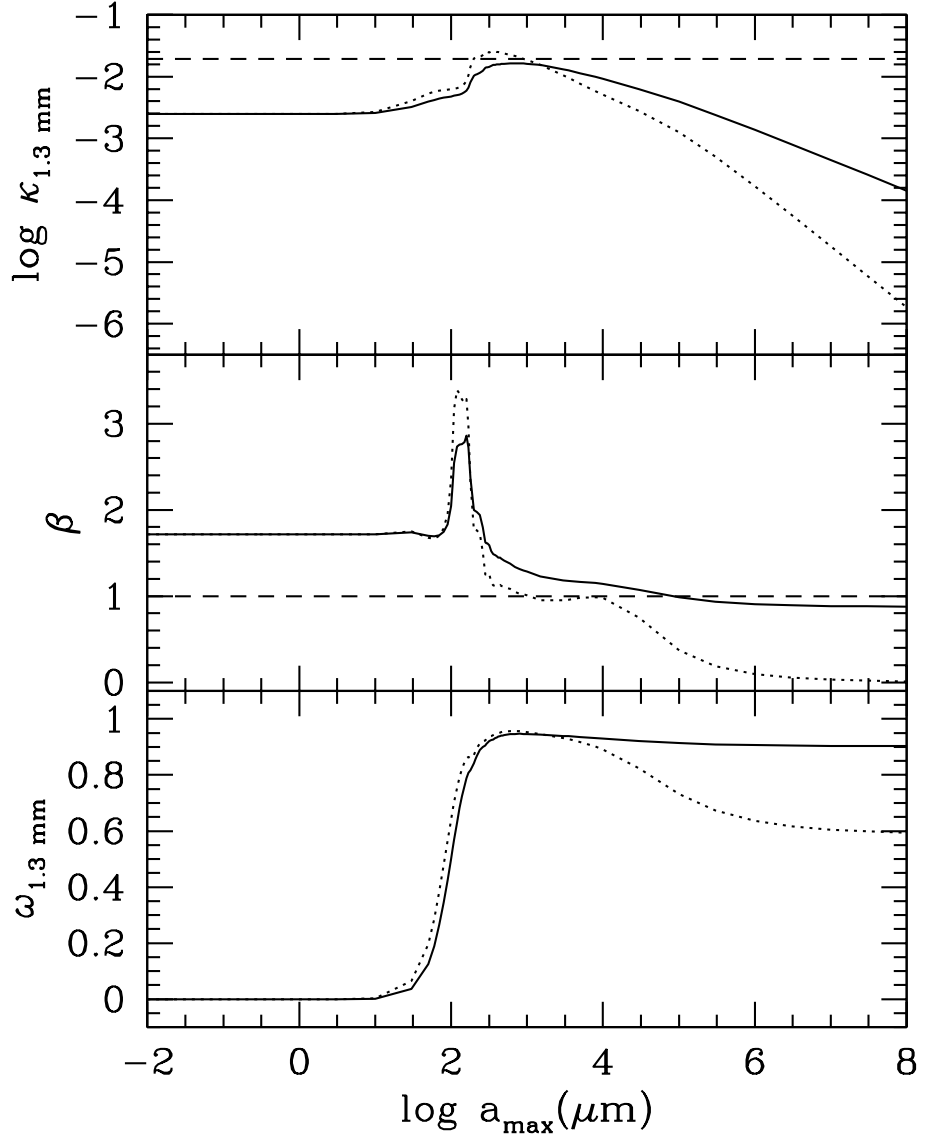


Fig. 3.— Upper Panel: Mass absorption coefficient at $\lambda = 1.3$ mm as a function of the maximum grain radius a_{\max} . The solid line corresponds to $p = 3.5$ and the dotted line to $p = 2.5$. The horizontal dashed line represents the frequently adopted opacity at 1.3 mm from BS91. Middle panel: $\beta = d \log(\kappa_{\nu})/d \log(\nu)$, calculated between $\lambda = 0.769$ and 1.3 mm for the same cases as the upper panel. The horizontal dashed line is $\beta = 1$. Lower panel: albedo at 1.3 mm for the same cases shown in the upper panel.

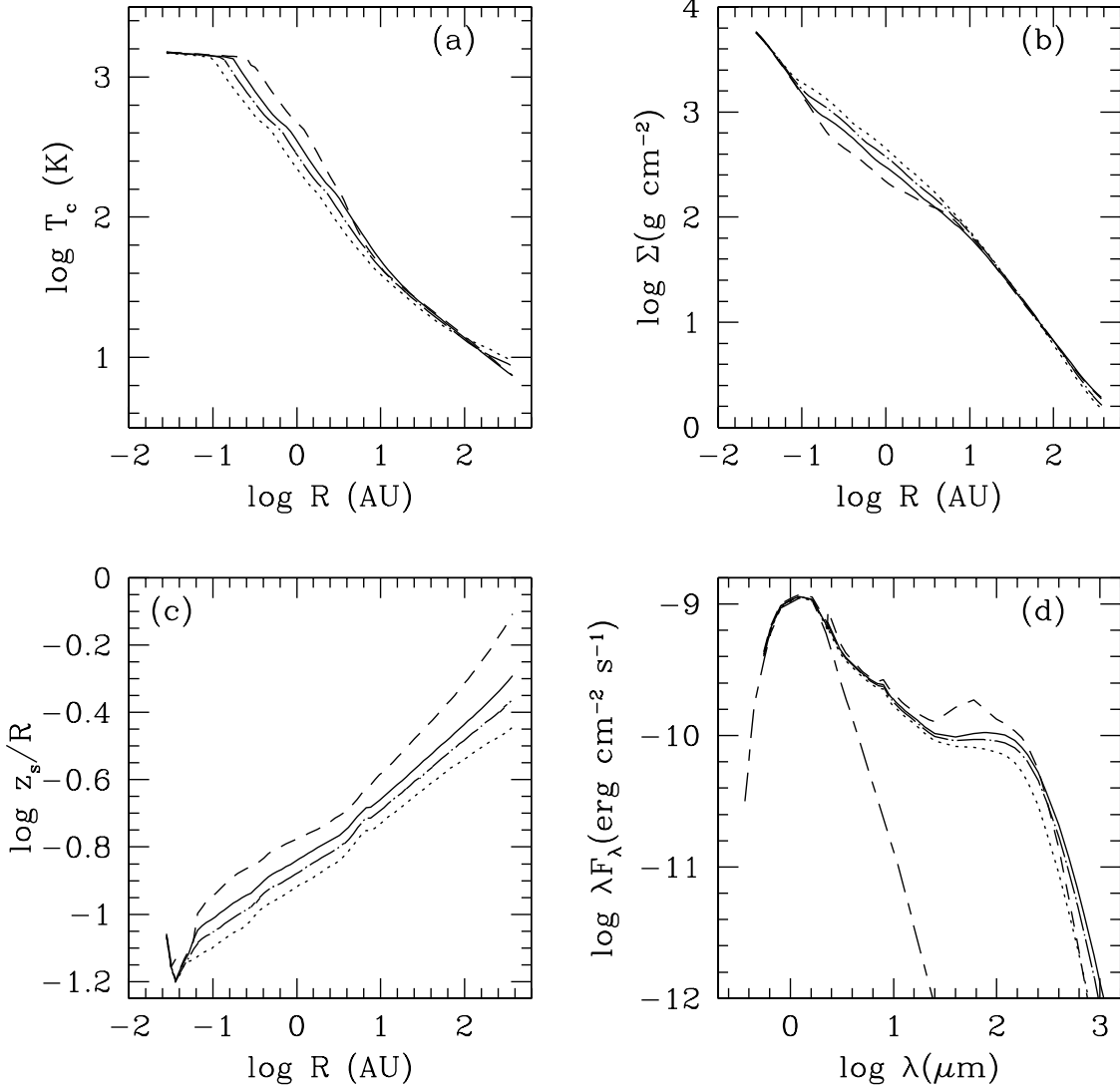


Fig. 4.— Disk structure and SED for different maximum grain size and exponent $p=3.5$. Each curve corresponds to a different value of maximum grain radius, $a_{max} = 10 \mu\text{m}$ (dashed line), 1 mm (solid line), 1 cm (dot-dashed line) and 10 cm (dotted line). Each panel represents the radial distribution of: (a) Midplane temperature; (b) Mass surface density; (c) Height of the irradiation surface divided by radius. In panel (d) the resulting SEDs are shown, assuming the disks are oriented pole-on. The SED of the central star is also plotted (long-short dashed line).

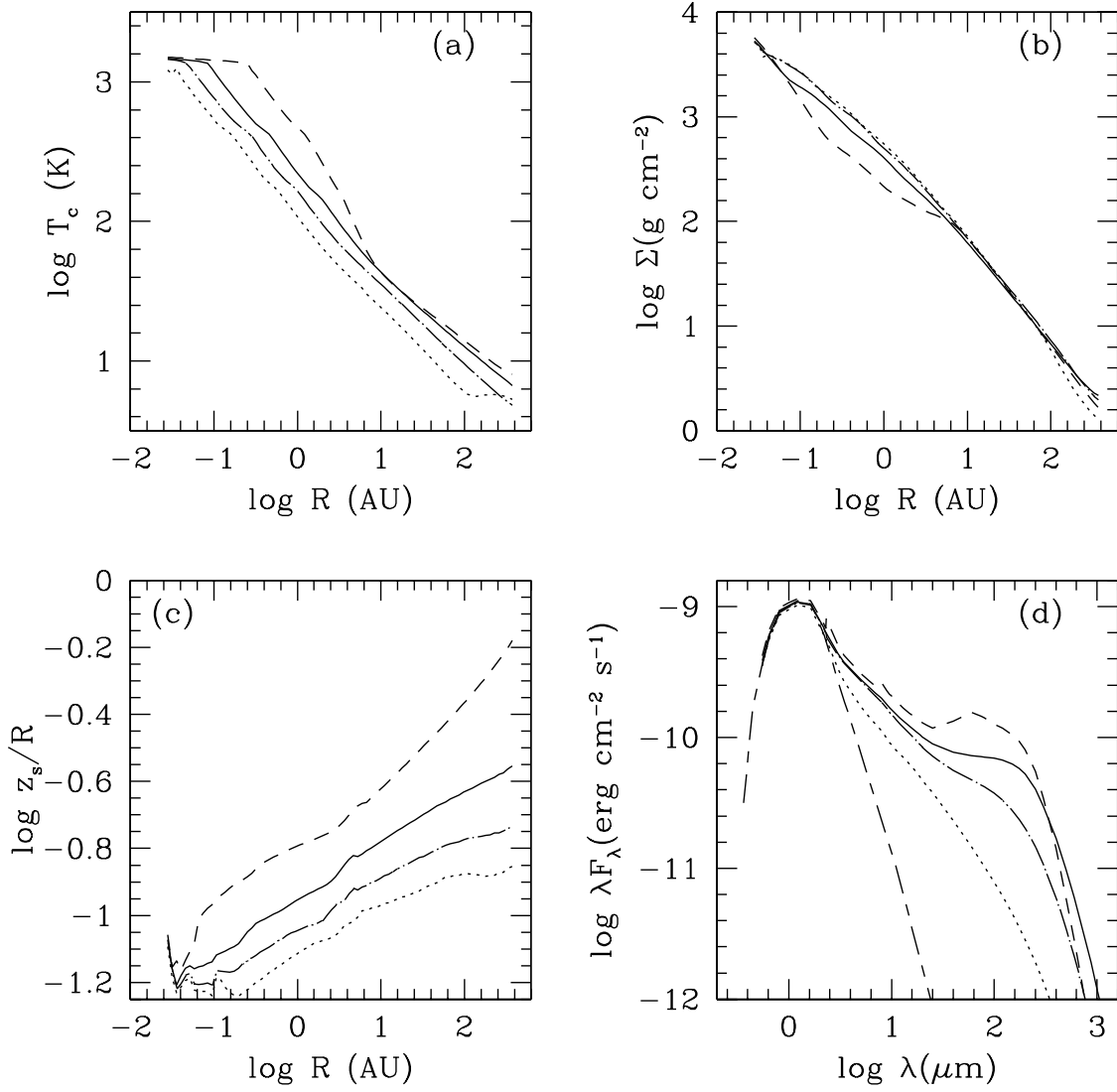


Fig. 5.— Disk structure and SED for different maximum grain size and exponent $p=2.5$. See caption of Figure 4.

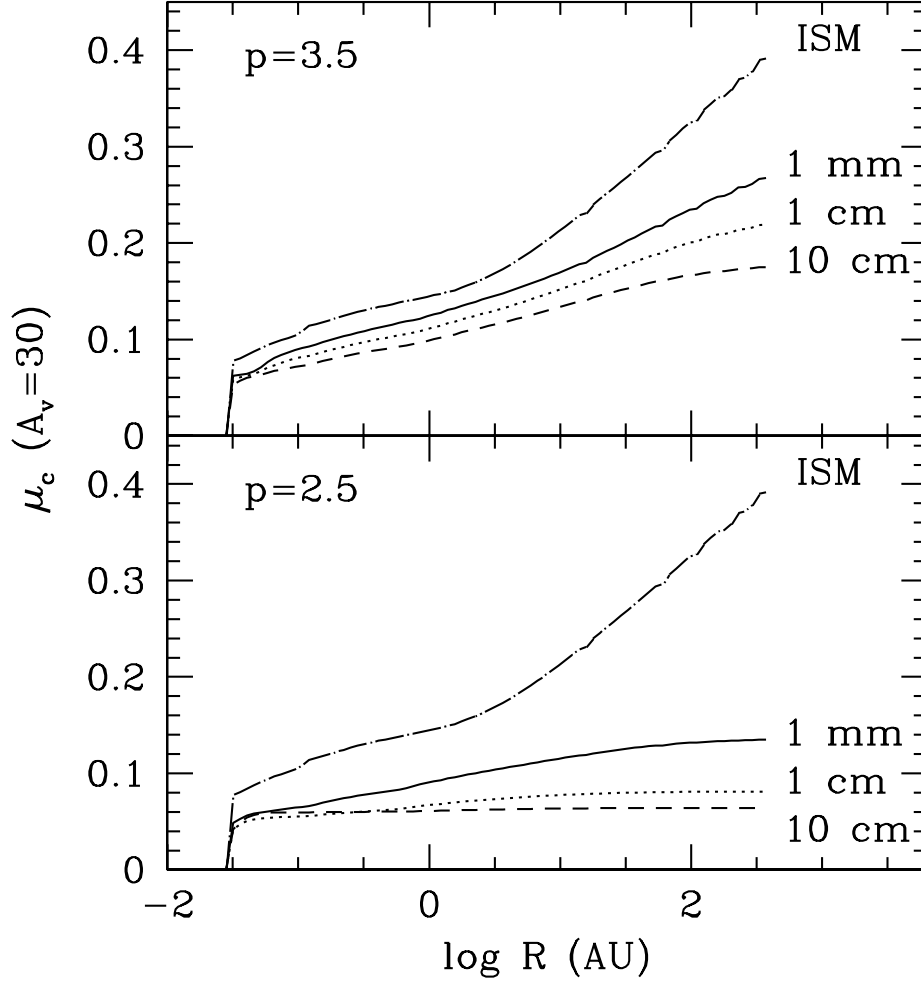


Fig. 6.— Cosine of critical inclination angle for disks models with $M_d = 0.046 M_\odot$ ($\dot{M} = 3 \times 10^{-8} M_\odot \text{yr}^{-1}$, $\alpha = 0.01$). The surface is defined so the extinction of the central star produced by the disk is $A_V = 30$, for dust abundances and optical properties described in §2 and different distributions of grain sizes: $a_{max} = 1 \text{ mm}$ (solid line), 1 cm (dotted line) and 10 cm (dashed line). The upper panel corresponds to $p = 3.5$ and the lower panel, to $p = 2.5$. For comparison we also show μ_c for ISM-dust, with ingredients and optical properties from Draine & Lee (1984), $p = 3.5$, $a_{max} = 0.25 \mu\text{m}$ (dot-dashed line).

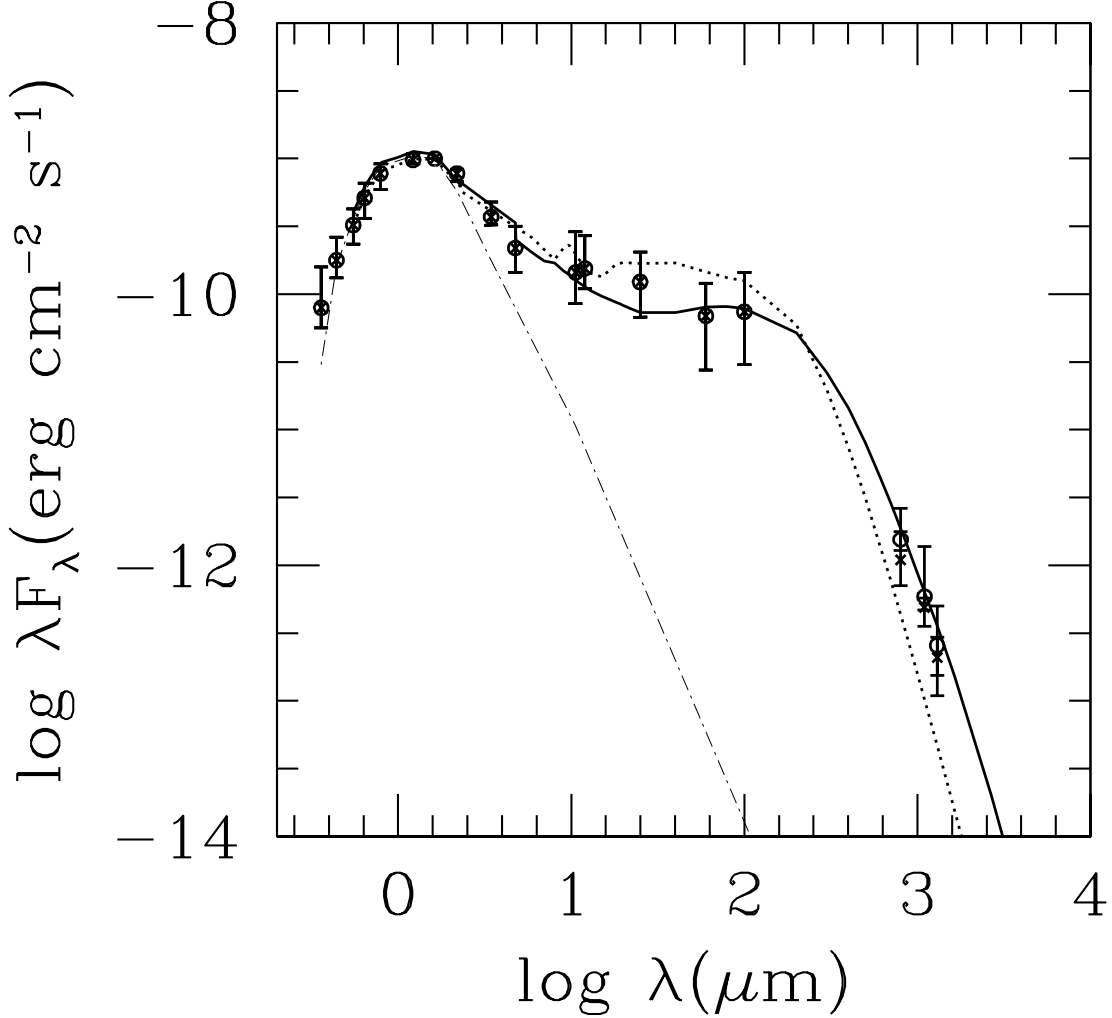


Fig. 7.— SED of the model with $M_d = 0.046 M_\odot$, $\dot{M} = 3 \times 10^{-8} M_\odot \text{ yr}^{-1}$, $\cos i = 0.65$, $R_d = 100$ AU, for ISM-dust (dotted line) and for the dust model adopted in this paper, with $p = 3.5$ and $a_{max} = 1$ mm (solid line). The points represent the median observed SED and the errorbars are the quartiles. The observed fluxes are normalized at $\lambda = 1.6 \mu\text{m}$. For the mm wavelengths we also show the median fluxes without normalization (crosses) (normalization is a reasonable procedure for optically thick emission, but since the mm flux could have an important contribution from optically thin region, the true mm median would be something between the normalized and the non normalized fluxes). The contribution of the UV and optical excess emission produced in an accretion shock is not included in the model SEDs.

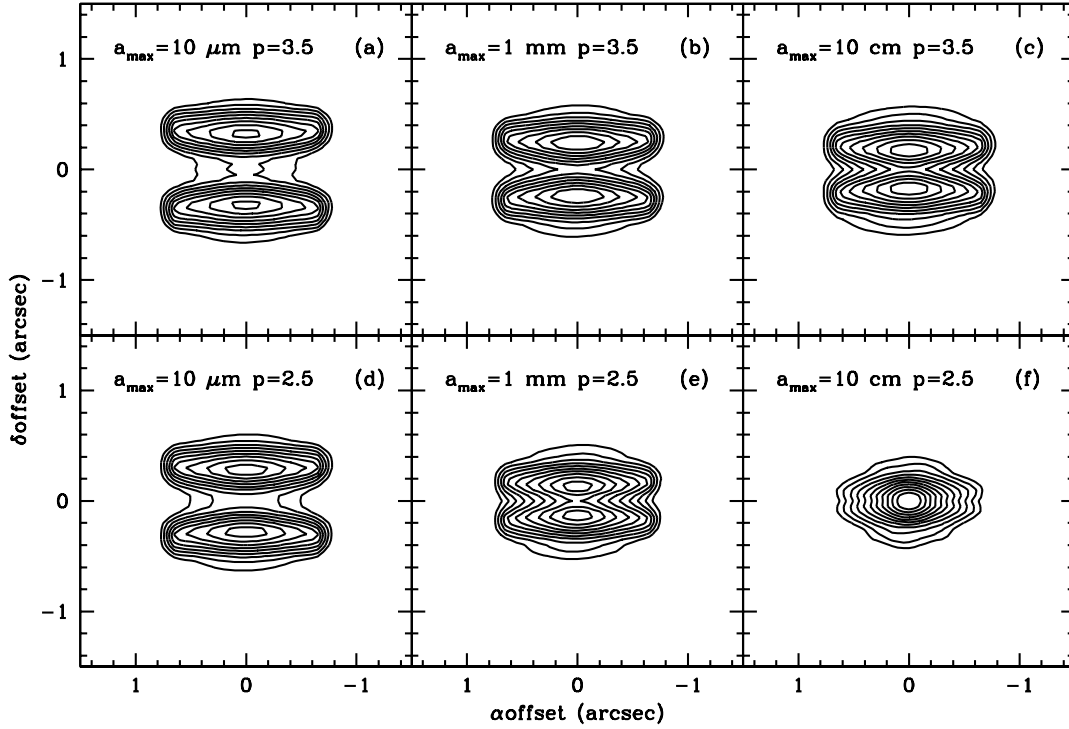


Fig. 8.— Images of edge-on disks at $\lambda = 0.814 \mu m$ for dust mixtures with $p=3.5$ (upper panels) and $p=2.5$ (lower panels), and $a_{max} = 10 \mu m$ (left), $a_{max} = 1 mm$ (center), and $a_{max} = 10 cm$ (right). The model has $M_d = 0.046 M_\odot$, and a central star with $L_* = 0.9 L_\odot$ and $T_* = 4000 K$. Each panel is labeled with the corresponding p and a_{max} . The images are calculated at $\lambda = 0.814 \mu m$ and convolved with the PSF of the HST PC1. The outermost contour level corresponds to $18.3 \text{ mag arcsec}^{-2}$, the peak contour level is $13.3 \text{ mag arcsec}^{-2}$, and the contour interval is $0.5 \text{ mag arcsec}^{-2}$.

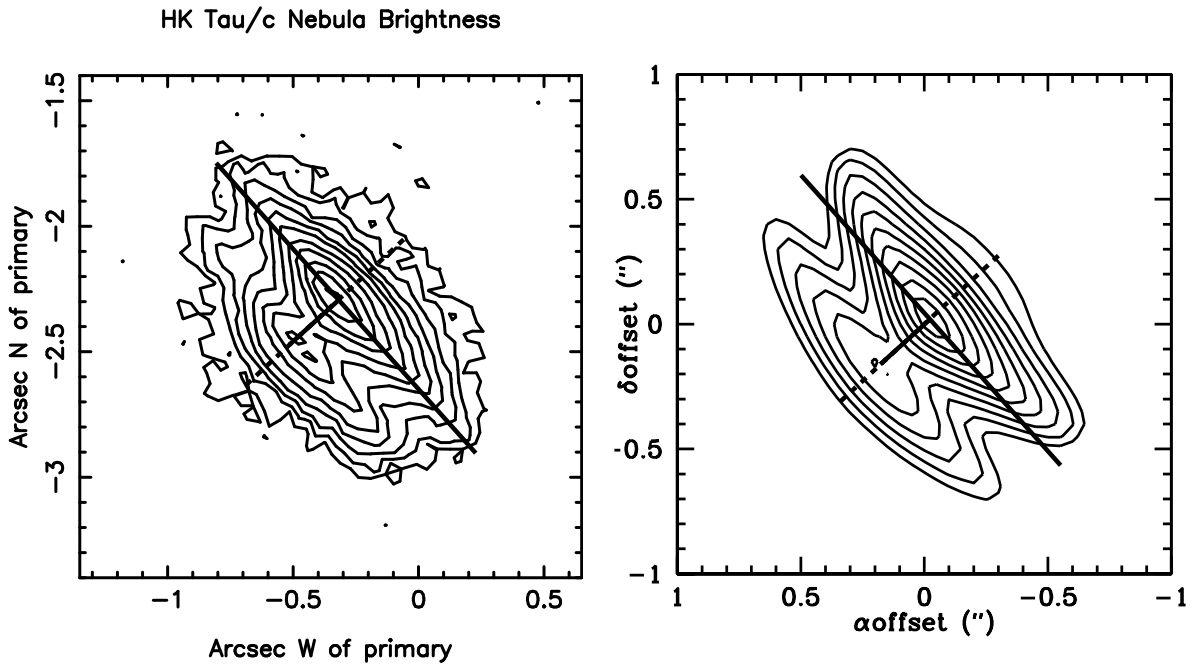


Fig. 9.— The left panel is the image of HK Tau/c (Stapelfeldt et al. 1998) and the right panel is the image of a disk model with $\dot{M} = 3 \times 10^{-8} M_{\odot} \text{ yr}^{-1}$, $\alpha = 0.01$, $R_d = 110 \text{ AU}$, $M_d = 0.065 M_{\odot}$, $M_* = 0.5 M_{\odot}$, $R_* = 1.3 R_{\odot}$, $T_* = 3500 \text{ K}$, $a_{max} = 1 \text{ m}$, $p = 3.5$. The disk inclination angle $i = 80.8^{\circ}$ and the P.A. is 40° . The levels are the same than in Figure 8 and in the observed image.

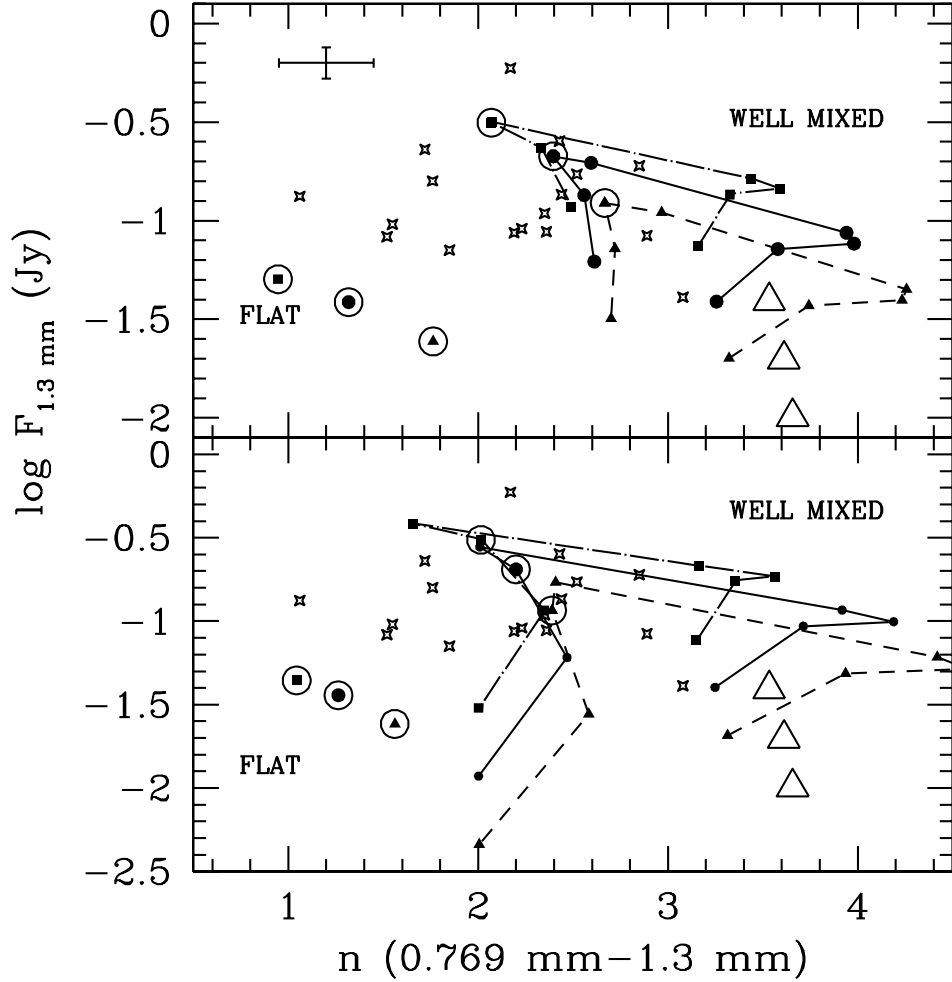


Fig. 10.— Model disk flux at 1.3 mm vs. spectral index n between 0.769 mm and 1.3 mm (lines) compared with observed values (stars) for Taurus from BSCG and BS91. Lines connect models of the same mass: $M_d \sim 0.023 M_\odot$ (dashed line), $M_d \sim 0.046 M_\odot$ (solid line), and $M_d \sim 0.092 M_\odot$ (dotted line). Model values are calculated for maximum grain sizes $a_{max} = 10, 100, 120, 150, 300 \mu\text{m}, 1 \text{ mm}, 1\text{cm}$ and 10 cm , identified by dots along the lines. For reference, the dot corresponding to $a_{max} = 1 \text{ mm}$ is encircled. Values for $a_{max} < 10 \mu\text{m}$ are similar to those for $a_{max} = 10 \mu\text{m}$. Upper panel: $p = 3.5$, lower panel: $p = 2.5$. Typical $1\text{-}\sigma$ errors are shown in the upper left corner of the upper panel. The range of α covered by each sequence of models is $\alpha = 0.02\text{-}0.04$ ($M_d \sim 0.023 M_\odot$), $\alpha = 0.01\text{-}0.02$ ($M_d \sim 0.046 M_\odot$), and $\alpha = 0.005\text{-}0.01$ ($M_d \sim 0.092 M_\odot$). We also show the flux and spectral index for flat irradiated models with the same masses, and $a_{max} = 1 \text{ mm}$ (circled dot, at the lower left corner) and for well mixed models with ISM-dust (big triangles).

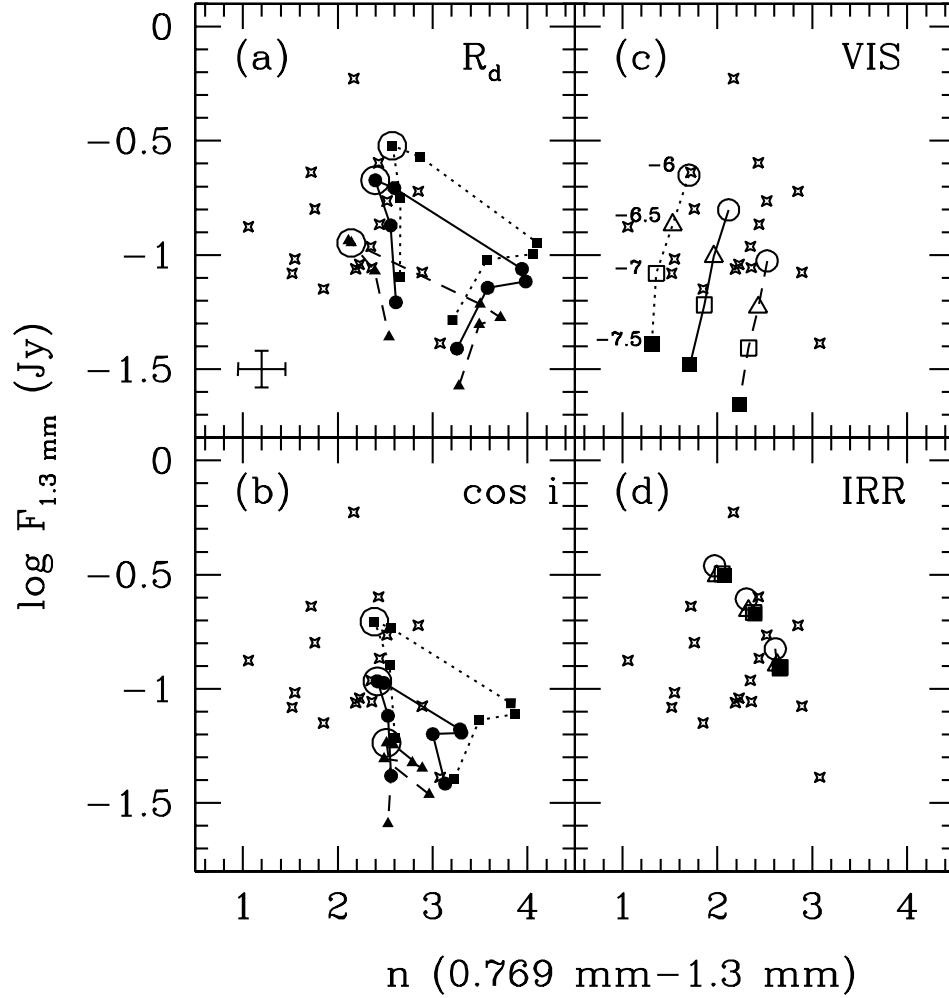


Fig. 11.— Model disk flux at 1.3 mm vs. spectral index n between 0.769 mm and 1.3 mm (lines) for different disk radius, inclination angle and mass accretion rate. (a) For the disk model with $p = 3.5$, $M_d \sim 0.046 M_\odot$ and $R_d = 100$ AU, we change the disk radius (and consequently the mass) keeping $\dot{M} = 3 \times 10^{-8} M_\odot \text{ yr}^{-1}$ and $\alpha = 0.01$. The plotted values are: $R_d = 50$ AU (dashed line), 100 AU (solid line) and 200 AU (dotted line). The values of a_{max} and the observations are described in Figure 10. (b) For the disk model with $p = 3.5$, $M_d \sim 0.046 M_\odot$ and $R_d = 100$ AU, we change the inclination angle, $\cos i = 0.25$ (dashed line), 0.5 (solid line) and 0.9 (dotted line). (c) Non irradiated viscous disks. Each symbol corresponds to a different mass accretion rate (labeled by $\log \dot{M}$) and the lines connect models with the same mass, $M_d = 0.092$ (dotted line), 0.046 (solid line) and 0.023 M_\odot (dashed line). For all these models $a_{max} = 1 \text{ mm}$, $p = 3.5$ and $i = 0^\circ$. (d) The same models shown in panel (c), irradiated by the central star (assuming dust and gas well mixed).

Table 1. Dust opacity and albedo

| a_{max} (μm) | p | T (K) | $\log \chi(0.8\mu m)$ | $\omega(0.8\mu m)$ | $\log \chi(0.769mm)$ | $\omega(0.769mm)$ | $\log \chi(1.3mm)$ | $\omega(1.3mm)$ | $\log \chi_p^*$ | $\log \kappa_p^*$ | $\log \chi_R$ | $\log \kappa_R$ | $\chi(0.55\mu m)/\chi(1\mu m)$ |
|-----------------------|-----|---------|-----------------------|--------------------|----------------------|-------------------|--------------------|-----------------|-----------------|-------------------|---------------|-----------------|--------------------------------|
| 1.00E-01 | 3.5 | 100 | +1.62E+00 | +3.18E-01 | -2.21E+00 | +7.53E-09 | -2.60E+00 | +2.26E-09 | +1.68E+00 | +1.44E+00 | +4.38E-01 | +7.21E-01 | 4.62E+00 |
| 1.00E+00 | 3.5 | 100 | +2.44E+00 | +9.02E-01 | -2.21E+00 | +6.29E-06 | -2.60E+00 | +1.88E-06 | +2.34E+00 | +1.42E+00 | +4.41E-01 | +7.25E-01 | 1.79E+00 |
| 1.00E+01 | 3.5 | 100 | +2.08E+00 | +8.91E-01 | -2.19E+00 | +5.76E-03 | -2.59E+00 | +1.73E-03 | +2.02E+00 | +1.13E+00 | +5.71E-01 | +8.04E-01 | 1.43E+00 |
| 1.00E+02 | 3.5 | 100 | +1.61E+00 | +8.85E-01 | -1.21E+00 | +7.68E-01 | -2.02E+00 | +5.00E-01 | +1.56E+00 | +6.89E-01 | +8.20E-01 | +5.78E-01 | 1.39E+00 |
| 1.00E+03 | 3.5 | 100 | +1.12E+00 | +8.84E-01 | -3.51E-01 | +9.29E-01 | -5.24E-01 | +9.46E-01 | +1.07E+00 | +2.08E-01 | +4.17E-01 | +1.30E-01 | 1.38E+00 |
| 1.00E+04 | 3.5 | 100 | +6.25E-01 | +8.84E-01 | -7.51E-01 | +9.06E-01 | -8.78E-01 | +9.31E-01 | +5.74E-01 | -2.85E-01 | -6.54E-02 | -3.57E-01 | 1.37E+00 |
| 1.00E+05 | 3.5 | 100 | +1.26E-01 | +8.84E-01 | -1.23E+00 | +8.89E-01 | -1.34E+00 | +9.14E-01 | +7.52E-02 | -7.81E-01 | -5.60E-01 | -8.53E-01 | 1.37E+00 |
| 1.00E+06 | 3.5 | 100 | -3.74E-01 | +8.84E-01 | -1.72E+00 | +8.84E-01 | -1.83E+00 | +9.06E-01 | -4.24E-01 | -1.28E+00 | -1.06E+00 | -1.35E+00 | 1.37E+00 |
| 1.00E-01 | 3.5 | 300 | +1.59E+00 | +2.67E-01 | -2.41E+00 | +7.36E-09 | -2.79E+00 | +2.13E-09 | +1.61E+00 | +1.41E+00 | +7.10E-01 | +8.35E-01 | 4.32E+00 |
| 1.00E+00 | 3.5 | 300 | +2.19E+00 | +8.28E-01 | -2.41E+00 | +6.15E-06 | -2.79E+00 | +1.78E-06 | +2.11E+00 | +1.40E+00 | +7.98E-01 | +8.65E-01 | 1.61E+00 |
| 1.00E+01 | 3.5 | 300 | +1.79E+00 | +7.86E-01 | -2.39E+00 | +5.52E-03 | -2.76E+00 | +1.60E-03 | +1.73E+00 | +1.10E+00 | +1.03E+00 | +8.54E-01 | 1.42E+00 |
| 1.00E+02 | 3.5 | 300 | +1.31E+00 | +7.71E-01 | -1.35E+00 | +7.33E-01 | -2.16E+00 | +4.39E-01 | +1.26E+00 | +6.52E-01 | +7.48E-01 | +4.72E-01 | 1.39E+00 |
| 1.00E+03 | 3.5 | 300 | +8.19E-01 | +7.67E-01 | -6.82E-01 | +8.80E-01 | -8.44E-01 | +9.03E-01 | +7.68E-01 | +1.67E-01 | +2.80E-01 | -3.36E-03 | 1.38E+00 |
| 1.00E+04 | 3.5 | 300 | +3.21E-01 | +7.66E-01 | -1.10E+00 | +8.58E-01 | -1.22E+00 | +8.88E-01 | +2.70E-01 | -3.27E-01 | -2.11E-01 | -4.94E-01 | 1.38E+00 |
| 1.00E+05 | 3.5 | 300 | -1.78E-01 | +7.66E-01 | -1.58E+00 | +8.47E-01 | -1.69E+00 | +8.75E-01 | -2.28E-01 | -8.21E-01 | -7.08E-01 | -9.84E-01 | 1.38E+00 |
| 1.00E+06 | 3.5 | 300 | -6.78E-01 | +7.65E-01 | -2.07E+00 | +8.44E-01 | -2.18E+00 | +8.70E-01 | -7.24E-01 | -1.31E+00 | -1.21E+00 | -1.46E+00 | 1.38E+00 |
| 1.00E-01 | 2.5 | 100 | +1.74E+00 | +4.42E-01 | -2.21E+00 | +1.38E-08 | -2.60E+00 | +4.14E-09 | +1.81E+00 | +1.46E+00 | +4.38E-01 | +7.21E-01 | 5.15E+00 |
| 1.00E+00 | 2.5 | 100 | +2.54E+00 | +9.29E-01 | -2.21E+00 | +1.36E-05 | -2.60E+00 | +4.09E-06 | +2.43E+00 | +1.38E+00 | +4.43E-01 | +7.30E-01 | 1.32E+00 |
| 1.00E+01 | 2.5 | 100 | +1.66E+00 | +8.68E-01 | -2.18E+00 | +1.26E-02 | -2.57E+00 | +3.80E-03 | +1.65E+00 | +8.02E-01 | +6.51E-01 | +8.40E-01 | 1.01E+00 |
| 1.00E+02 | 2.5 | 100 | +6.61E-01 | +8.41E-01 | -8.68E-01 | +8.35E-01 | -1.76E+00 | +6.41E-01 | +6.61E-01 | -6.79E-02 | +6.16E-01 | +2.86E-01 | 9.98E-01 |
| 1.00E+03 | 2.5 | 100 | -3.42E-01 | +8.33E-01 | -3.65E-01 | +9.28E-01 | -4.04E-01 | +9.53E-01 | -3.41E-01 | -9.88E-01 | -3.36E-01 | -6.88E-01 | 9.98E-01 |
| 1.00E+04 | 2.5 | 100 | -1.34E+00 | +8.31E-01 | -1.32E+00 | +8.19E-01 | -1.32E+00 | +8.92E-01 | -1.34E+00 | -1.91E+00 | -1.34E+00 | -1.70E+00 | 9.99E-01 |
| 1.00E+05 | 2.5 | 100 | -2.35E+00 | +8.30E-01 | -2.33E+00 | +6.72E-01 | -2.33E+00 | +7.32E-01 | -2.26E+00 | -2.69E+00 | -2.34E+00 | -2.71E+00 | 1.00E-00 |
| 1.00E+06 | 2.5 | 100 | -3.35E+00 | +8.30E-01 | -3.34E+00 | +6.16E-01 | -3.34E+00 | +6.36E-01 | -2.86E+00 | -3.02E+00 | -3.34E+00 | -3.72E+00 | 1.00E-00 |
| 1.00E-01 | 2.5 | 300 | +1.70E+00 | +3.83E-01 | -2.41E+00 | +1.35E-08 | -2.79E+00 | +3.90E-09 | +1.74E+00 | +1.44E+00 | +7.10E-01 | +8.36E-01 | 4.75E+00 |
| 1.00E+00 | 2.5 | 300 | +2.20E+00 | +8.46E-01 | -2.41E+00 | +1.33E-05 | -2.79E+00 | +3.86E-06 | +2.14E+00 | +1.35E+00 | +4.46E-01 | +8.93E-01 | 1.12E+00 |
| 1.00E+01 | 2.5 | 300 | +1.27E+00 | +6.77E-01 | -2.36E+00 | +1.18E-02 | -2.74E+00 | +3.46E-03 | +1.26E+00 | +7.62E-01 | +1.07E+00 | +7.92E-01 | 1.00E+00 |
| 1.00E+02 | 2.5 | 300 | +2.60E-01 | +6.00E-01 | -1.01E+00 | +8.01E-01 | -1.91E+00 | +5.72E-01 | +2.61E-01 | -1.37E-01 | +2.57E-01 | -7.26E-02 | 9.95E-01 |
| 1.00E+03 | 2.5 | 300 | -7.48E-01 | +5.77E-01 | -7.55E-01 | +8.71E-01 | -7.83E-01 | +9.07E-01 | -7.41E-01 | -1.11E+00 | -7.41E-01 | -1.08E+00 | 9.97E-01 |
| 1.00E+04 | 2.5 | 300 | -1.75E+00 | +5.69E-01 | -1.73E+00 | +7.69E-01 | -1.72E+00 | +8.45E-01 | -1.70E+00 | -2.01E+00 | -1.75E+00 | -1.99E+00 | 9.99E-01 |
| 1.00E+05 | 2.5 | 300 | -2.75E+00 | +5.66E-01 | -2.74E+00 | +6.73E-01 | -2.73E+00 | +7.22E-01 | -2.40E+00 | -2.53E+00 | -2.75E+00 | -2.47E+00 | 1.00E-00 |
| 1.00E+06 | 2.5 | 300 | -3.75E+00 | +5.66E-01 | -3.75E+00 | +6.41E-01 | -3.75E+00 | +6.58E-01 | -2.62E+00 | -2.65E+00 | -3.75E+00 | -2.57E+00 | 1.00E-00 |
| 2.50E-01 | 3.5 | 100 | +1.94E+00 | +5.46E-01 | -2.51E+00 | +9.72E-08 | -2.97E+00 | +3.45E-08 | +1.84E+00 | +1.51E+00 | -1.43E-01 | +1.50E-01 | 2.46E+00 |
| 2.50E-01 | 3.5 | 300 | +1.94E+00 | +5.46E-01 | -2.51E+00 | +9.72E-08 | -2.97E+00 | +3.45E-08 | +1.84E+00 | +1.51E+00 | +4.66E-01 | +6.28E-01 | 2.46E+00 |